A soft robotic sleeve mimicking the haemodynamics and biomechanics of left ventricular pressure overload and aortic stenosis

Luca Rosalia[1,2,3,4,&], Caglar Ozturk[2,&], Jaume Coll-Font[3,4], Yiling Fan[2,3,4,5], Yasufumi Nagata[6,7], Manisha Singh[2], Debkalpa Goswami[2], Adam Mauskapf[8], Shi Chen[3,4], Robert A. Eder[3,4], Efrat M. Goffer[1,2], Jo H. Kim[3,4], Salva Yurista[3,4], Benjamin P. Bonner[3,4], Anna N. Foster[3,4], Robert A. Levine[6,7], Elazer R. Edelman[1,2,9], Marcello Panagia[3,10], Jose L. Guerrero[3], Ellen T. Roche[1,2,5,*], Christopher T. Nguyen[1,3,4,7,11,*]

[1]Health Sciences and Technology Program, Harvard - Massachusetts Institute of Technology, 77 Massachusetts Avenue, Cambridge, MA 02139, USA

[2]Institute for Medical Engineering and Science, Massachusetts Institute of Technology, 45 Carleton Street, Cambridge, MA 02139, USA

[3]Cardiovascular Research Center, Massachusetts General Hospital, 149 13th Street, Charlestown, MA 02129, USA

[4]A.A. Martinos Center for Biomedical Imaging, Massachusetts General Hospital, 149 13th Street Charlestown, MA 02129, USA

[5]Department of Mechanical Engineering, Massachusetts Institute of Technology, 33 Massachusetts Avenue, Cambridge, MA 02139, USA

[6]Cardiac Ultrasound Laboratory, Massachusetts General Hospital, 55 Fruit Boston, MA 02114, USA

[7]Department of Medicine, Harvard Medical School, 25 Shattuck Street, Boston, MA 02115, USA

[8]Corrigan Minehan Heart Center, Massachusetts General Hospital, Boston, 55 Fruit Boston, MA 02114, USA

[9]Brigham and Women's Hospital, Cardiovascular Division, 75 Francis Street, Boston, MA 02115, USA

[10]Cardiovascular Medicine Section, Department of Medicine, Boston University Medical Center, 715 Albany Street, Boston, MA 02118, USA

[11]Cardiovascular Innovation Research Center, Heart, Vascular, and Thoracic Institute, Cleveland Clinic, 9500 Euclid Ave, Cleveland, OH 44195, USA

Abstract

Preclinical models of aortic stenosis can induce left ventricular pressure overload and coarsely control the severity of aortic constriction. However, they do not recapitulate the haemodynamics and flow patterns associated with the disease. Here, we report the development of a customizable soft robotic aortic sleeve that can mimic the haemodynamics and biomechanics of aortic stenosis. By allowing for the adjustment of actuation patterns and blood-flow dynamics, the robotic sleeve recapitulates clinically relevant haemodynamics in a porcine model of aortic stenosis, as we show by means of in vivo echocardiography and catheterization studies and via a combination of in vitro and computational analyses. We also quantified, by means of in vivo and in vitro magnetic resonance imaging, the four-dimensional blood-flow velocity profiles associated with the disease and with bicommissural and unicommissural defects recreated by the robotic sleeve. The design of the sleeve, which can be adjusted on the basis of computer-tomography data, allows for the design of patient-specific devices that may guide clinical decisions and improve the management and treatment of patients with aortic stenosis.

Advances in soft robotics have led to the development of high-fidelity simulators of pathophysiology for biomedical applications[1]. By using materials with mechanical properties similar to those of biological tissues, soft robotic actuators are capable of recapitulating the biomechanical function and complex motion dynamics of various organ systems, including the heart[2], the gastrointestinal tract[3,4], the respiratory system[5,6] and others[7,8]. These simulators could serve as systems for the development and testing of medical therapies, treatment planning, and studies of human physiology and disease. However, they can only model organ systems in isolation, failing to capture the complex physiologic interplay arising, for example, from neurohormonal control and feedback or compensation mechanisms. Here, we present an *in vivo* disease model that uses a biomimetic soft robotic sleeve to recapitulate the haemodynamics of aortic stenosis (AS) in swine, and describe the use of computational tools and 4D magnetic resonance imaging (MRI), among other techniques, to validate its haemodynamic mimicry.

AS is an obstruction of blood flow through the aortic valve mediated by calcification and inflammatory processes, often caused by congenital aortic valve defects[9–11]. Owing to the association between age and AS and the progressive aging of the population, the global prevalence of AS has increased approximately from 2 to 9 million in the past three decades[12,13]. Correspondingly, global deaths rose from 50 to 120 thousand in the same period[13]. If untreated, AS can result in heart failure[11,14–16] and sudden death[17]. High-fidelity *in vivo* models of AS may advance the development of risk stratification frameworks to guide the management of AS in patient groups for whom interventional guidelines remain heterogeneous, including i) asymptomatic patients with severe dynamic markers of AS and ii) symptomatic patients with mildly abnormal haemodynamics[11,18–20]. We believe

that the development of high-fidelity models of AS may eventually pave the way towards personalized AS management, improving perioperative mortality rates of AS interventions and patient outcome.

The majority of former *in vivo* models of AS use rigid bands or inflatable cuffs around the ascending aorta to induce left ventricular (LV) pressure overload[21–23]. These devices can only achieve simple concentric-like constriction of the aorta and fail to recreate the complex 3D flow patterns observed in AS created by maladaptive geometry from calcification or congenital defects of leaflet valves. Moreover, their limited control prevents them from recapitulating the haemodynamics of congenital aortic valve defects, which often accelerate the onset and progression of AS, as well as aortic remodelling, potentially leading to other complications including aortic aneurysms, dissection, and regurgitation[24]. In this work, we focus on recreating the haemodynamics of calcific AS, as well as of bicuspid or bicommissural aortic valve (BAV) – the most common congenital valve disease [11,25,26] – and unicommissural aortic valve (UAV) – a rare congenital defect that is typically associated with an even poorer prognosis than BAV[27–29].

Here, we report the development of a highly tuneable and dynamic biomimetic soft robotic aortic sleeve that recapitulates the haemodynamics of pressure overload secondary to AS and enables biomechanical mimicry of stenotic aortic valves. With the potential to recreate patient-specific haemodynamic profiles by customization of the actuation scheme or sleeve geometry, the proposed sleeve demonstrates the development of high-fidelity, tuneable *in vivo* models of human disease (Fig. 1a). This biomimetic soft robotic technology is poised to model a broader spectrum of human diseases, paving the way towards other medical applications including studies of vascular valve stenosis (that is, carotid, peripheral arterial disease, aortic coarctation) or pulmonary valve stenosis, urinary or gastrointestinal sphincter dysfunction, and airway obstruction. These models could therefore provide insights into a wide range of pathophysiological conditions and support translational research by guiding innovation in medical devices and therapies.

Design of a biomimetic soft robotic aortic sleeve

A highly tuneable biomimetic soft robotic aortic sleeve is composed of three expandable elements or pockets, each connected to one actuation line. An inelastic fabric sheet spanning across the base of the soft actuator restrains the expansion of the pockets to one direction under pressure and a slit and strip mechanism allows positioning around the outer wall of the porcine aorta. The expandable bladder is made of two vacuum-formed sheets of thermoplastic polyurethane (TPU) and a TPU-coated nylon fabric is used as the constraining layer. A positive and a negative mould of the bladder were made for vacuum-forming and sealing of the expandable elements respectively (Fig. 1b,c). Fig. 1d illustrates the mechanical response to uniaxial loading of the TPU and nylon layers. 3D representations of the sleeve with details of the TPU pockets, the constraining layer, and the actuation lines are shown in Fig. 1e,f (see Supplementary Note 1: Aortic sleeve manufacture and Supplementary Fig. 1). Histology studies on each of the materials constituting the aortic sleeve resulted in minimal fibrous tissue and no notable lymphocytic infiltrates (see Supplementary Note 2: Histology studies and Supplementary Fig. 2). Fig. 1g shows

the position of the biomimetic sleeve around the ascending aorta of the human heart finite element (FE) model (Living Heart Project Abaqus 2018, SIMULIA™, Dassault Systèmes®)[30].

The soft robotic sleeve can be actuated under hydraulic quasi-static volume-control conditions or under pneumatic dynamic pressure control. Both quasi-static and dynamic actuations allow us to recapitulate the haemodynamics of LV pressure overload. However, while quasi-static actuation is better suited to create longitudinal models of progressive pressure overload, dynamic control enables high-fidelity biomechanical and haemodynamic mimicry of a stenotic aortic valve and is therefore poised to create pressure overload models secondary to AS. Further, patient-specific aortic flow patterns can be recreated with enhanced accuracy compared to other models. By enabling actuation dynamics and pressure levels independently for each pocket of the sleeve during both systole and diastole (Supplementary Video 1), our biomimetic sleeve allows the recreation of a variety of kinematics of stenotic aortic valves that could be relevant for preclinical and translational studies of human physiology and disease.

In vitro and in silico modelling of the biomimetic sleeve

We characterized the mechanical behaviour and haemodynamic effects of the biomimetic soft robotic sleeve using a combination of *in vitro* and *in silico* methods. Fig. 2a illustrates the axial forces generated by the sleeve upon dynamic (pressure-control) and quasi-static (volume-control) actuation as measured by electromechanical tester. Using a mock circulatory loop (MCL) and a FE simulation, we could predict the global haemodynamics resulting from actuation of the biomimetic soft robotic aortic sleeve (Fig. 2b–e). The FE model was adapted from the Living Heart Model (Abaqus 2018, SIMULIA™, Dassault Systèmes®)[30]. Both the *in vitro* and the *in silico* models were tuned to approximate the porcine haemodynamics measured *in vivo* at baseline (Supplementary Table 1). In addition, the *in vitro* MCL loop was simplified and readapted to the magnetic resonance (MR) environment enabling visualization of the flow and velocity vector fields upon sleeve actuation (Fig. 2f,g).

Both the *in vitro* and *in silico* models show consistent results with clinical literature[31,32] in that actuation of the sleeve results in a drop in the effective orifice area (EOA) from baseline (BL) (Fig. 2b) and in corresponding elevations in the maximum (P_{max}; Fig. 2c) and mean (P_{mean}; Fig. 2d) transaortic pressure gradients, and an increase in the peak LV pressure (LVP_{max}; Fig. 2e). As more comprehensively demonstrated by the *in vivo* results presented hereafter, these *in vitro* and *in silico* studies show the soft robotic aortic sleeve can induce haemodynamic changes associated with different degrees of AS, from mild to severe. Further, the magnitude of these changes is increasingly more prominent at elevated actuation pressures. Analogously, LV pressure-volume (PV) loops obtained *in silico* (Fig. 2f) illustrate increases in the peak LV pressure, in agreement with clinical and computational studies of AS and pressure overload [11,33,34,35]. Any discrepancy between the *in vitro* and *in silico* predictions can likely be attributed to slight differences in the definition of lumped-parameter elements and the dynamic response of the aortic material definition of the FE simulation with respect to the MCL set-up.

Dynamic MRI of the simplified *in vitro* system illustrates the flow velocity vector map along a longitudinal cut of the mock aortic vessel and on the cross-sectional plane in correspondence to the sleeve (Fig. 2g,h). These images illustrate changes in the velocity due to actuation of the sleeve, with peak velocities achieved in the centre of the sleeve plane, where the cross-sectional area is reduced. In Fig. 2g,h, changes in velocity along the direction of flow are exemplified by velocity profile plots at three distinct planes along the vessel. These plots further demonstrate that flow velocity peaks at the sleeve plane and subsequently drops downstream due to the obstruction to flow induced by the sleeve. Additionally, Womersley flow can be observed in the downstream plane when the sleeve is not actuated, whereas complex flow patterns, including vorticity formation, result from actuation.

In vivo study design and overview

To demonstrate the functionality of the sleeve *in vivo*, we implanted the aortic sleeve in seven Yorkshire pigs of weight ranging between 38 and 45kg (see Supplementary Note 3: In vivo studies). Of the seven swine, one swine was euthanized due to severe cardiac effusion with haemodynamic repercussions observed on MRI, and two swine were excluded from the analysis due to under-tensioning of the sleeve during implantation (Extended Data Fig. 1 a,b). Three swine successfully underwent quasi-static sleeve actuation, and the sleeve was actuated dynamically on one swine (Extended Data Fig. 1 c–f).

The timeline of the investigation is shown in Fig. 3a. Cardiac function was assessed at the beginning of the study (D0) on transthoracic echocardiography (TTE) prior to implantation. We evaluated cardiac function and aortic flow haemodynamics on MRI (D6) and performed LV catheterization and transepicardial echocardiography as a terminal procedure eight days post implantation (D8). For all studies, we actuated the sleeve immediately prior to haemodynamic evaluation, and released it following data acquisition. In quasi-static studies, due to the prolonged time required for MRI image acquisition and associated risks, we limited the severity of aortic constriction to approximately 3 mL during MRI studies.

Recapitulating the clinical metrics of AS

We measured the haemodynamics induced in swine acutely by actuation of the biomimetic soft robotic aortic sleeve at day 8 (D8). Supplementary Table 1 provides a summary of the haemodynamics recorded at baseline, i.e., prior to actuation. *In vivo* results upon quasi-static and dynamic actuation are shown in Fig. 3b–j and Fig. 3k–m, respectively. Clinical metrics used for the diagnostic evaluation and staging of AS are shown in (Fig. 3b–g), including the indexed effective orifice area (iEOA), P_{max}, P_{mean}, peak jet flow velocity (v_{max}), energy loss index (ELI), and valvulo-arterial impedance (Z_{VA}), with thresholds of mild, moderate, and severe AS[31,32,36–38]. Specifically, the iEOA (Fig. 3b) and ELI (Fig. 3f) drop with sleeve actuation, whereas P_{max} (Fig. 3c), P_{mean} (Fig. 3d), v_{max} (Fig. 3e), and Z_{VA} (Fig. 3g) increase. These results illustrate that actuation of the sleeve can recapitulate the global haemodynamics associated with AS for each of the severity levels of disease. Table 1 shows that actuation of the biomimetic soft robotic sleeve with actuation volumes lower than 2.0 – 2.6 mL or greater than 2.8 – 3.7 mL induces haemodynamics typical of those

seen in mild and severe AS respectively, with intermediate volumes resulting in changes associated with moderate AS. In addition, the progression of LV haemodynamics during one quasi-static actuation (Fig. 3h) shows an increase in afterload due to aortic constriction, and corresponding elevations in the LVP_{max} (Fig. 3i) and drops in the SV (Fig. 3j). Notably, while the rise in LVP_{max} is almost linear with respect to iEOA, the SV drops increasingly more rapidly at elevated values of iEOA.

Analogous changes in LV haemodynamics were observed upon dynamic actuation of the sleeve. Representative PV loops at BL, 6 and 8psi are shown in Fig. 3k, highlighting a similar progression of the ESPVR and EDPVR, as well as of the LVP_{max} (Fig. 3l) and SV (Fig. 3m).

Recreating aortic flow in AS and congenital valvular defects

The morphology of aortic constriction can be tuned by varying the actuation scheme of the three pockets of the sleeve, by customizing the sleeve design, or a combination thereof. This enables the recreation of patient-specific AS lesions and therefore has the potential to recreate patient-specific haemodynamics in an *in vivo* model, with profound clinical and translational implications.

The three expandable elements or pockets composing the sleeve are connected to three independent actuation lines. Activation of one pocket mimics fusion or stiffening of one corresponding commissure – the area where the valve leaflets abut. As a result, selective activation of the pockets of the aortic sleeve results in various constriction profiles. Specifically, actuation of all the three pockets leads to stiffening or partial fusion of the three commissures, resulting in a calcific tricuspid AS morphology. Bicommissural and unicommissural profiles are instead obtained from actuation of one and two pockets respectively. Graphic illustrations of the aortic valve for each of these profiles in both the closed and open configurations are shown in Fig. 4a, while Fig. 4b depicts the number of active pockets corresponding to each condition.

MRI enabled structural and haemodynamic visualization for each constriction profile *in vitro* and *in vivo* (D6). Supplementary Video 2 shows MRI images of the sleeve under dynamic actuation for the *in vitro* set-up. Supplementary Video 3 demonstrates quasi-static actuation on echocardiography and dynamic actuation on MRI for the stenosis (i.e., 3 active pockets) constriction profile in swine. Fig. 4c illustrates cross-sectional images of the porcine aorta obtained via 2D cine MRI of the stenosis, bicommissural, and unicommissural profiles, as well as the profiles obtained for each actuation scheme *in vitro*. The *in vivo* images include details of the pockets being actuated for each condition.

In Fig 4d, we report 2D velocity vector maps of a longitudinal section of the aorta for the three actuation profiles as well as the corresponding flow velocity cross-sections at the ascending aorta (P1), aortic arch (P2), and descending aorta (P3) in areas of transitional flow. These results illustrate elevated velocities at the ascending aorta and aortic arch for each condition, and that the flow profile follows closely the morphologies obtained via cine MRI (Fig. 4c), with maximal velocities in the proximity of the geometrical centre of the P1

plane and, generally, in the peripheries of the P2 and P3 planes. In addition, the velocity vector maps suggest that higher vorticities are present at the aortic arch and that these are even more prominent for the bicommissural and unicommissural constriction profiles, translating to higher turbulence kinetic energy (TKE) (Extended Data Fig. 2), compared to the calcific AS morphology. This is in agreement with the clinical literature, which suggests that patients with congenital valve defects have higher peak TKE compared to stenotic tricuspid aortic valves, whose associated TKE is in turn higher than in patients with a healthy aortic valve[39,40]. A computational fluid dynamics (CFD) model (see Supplementary Note 4: Computational modelling and Supplementary Video 4) was implemented to predict aortic flow patterns and the TKE associated with each constriction profile (Extended Data Fig. 3). Further haemodynamic results from *in vivo* MRI studies under dynamic actuation of the biomimetic soft robotic aortic sleeve can be found in Extended Data Fig. 4. Other potential effects on global and local haemodynamics and on aortic compliance due to sleeve implantation in the presence or absence of the native aortic valve are illustrated in Extended Data Fig. 5 and discussed further in Supplementary Note 5: Impact of sleeve implantation and Supplementary Table 2.

Towards patient-specific modelling

The design of our soft robotic aortic sleeve can be customized to mimic the morphology of patient-specific AS lesions. In a proof-of-concept study, we used computed tomography (CT) data of one AS patient's aorta exhibiting narrowing from calcification and leveraged segmentation and other image processing techniques to obtain the patient-specific AS morphology. The design of the expandable element of the patient-specific sleeve could then be obtained by unwrapping the circular patient-specific AS geometry flat onto a plane, and the entire sleeve could be manufactured using the vacuum-forming and heat-pressing techniques described above (Fig. 5A).

In vitro testing of the patient-specific sleeve enabled visualization of the resulting aortic cross-section geometry, which demonstrated the ability of the sleeve to recreate the desired patient-specific AS morphology with high fidelity. The geometries resulting from use of a commercial band, the non-specific sleeve, and the patient-specific sleeve were compared with the patient-specific AS morphology using the Dice similarity coefficient (DSC)[41] for each of the three conditions (Fig. 5B). Findings demonstrate that the commercial band yields the lowest DSC (0.47), while the patient-specific sleeve results in the highest DSC value (0.78), with an additional improvement compared to the non-specific sleeve (0.72) (Fig. 5B). Closely recreating the geometry of patient-specific lesions could enable accurate patient-specific haemodynamic mimicry, paving the way towards studies personalized approaches in the diagnosis, management, and treatment of AS.

Discussion

High-fidelity models of human physiology and disease are poised to have important implications for human health and clinical medicine. Soft robotic technology has enhanced the accuracy of benchtop or biohybrid simulators that can recapitulate the biomechanics and function of a variety of organ systems[1]. Although animal models of human disease are not as

broadly documented in the scientific literature, attempts have been made to induce pressure overload secondary to AS – one of the most highly prevalent valvular heart diseases[21,23,42]. However, existing technologies that enable simple concentric-like aortic constriction fail to recreate the nuanced and complex aortic flow haemodynamics associated with AS. Further, they suffer from limited controllability, elevated mortality rates, and the inability to recapitulate the temporal haemodynamics of patient-specific lesions or congenital valve disease, which often accelerates symptoms of AS. These limitations emphasize the need for more comprehensive and representative models of this condition.

In this work, we describe the development of a high-fidelity *in vivo* model with primary utility for AS by means of a biomimetic soft robotic aortic sleeve. This is composed of expandable elements or pockets that can be individually activated to enable customization of aortic flow patterns. The sleeve can be actuated in a quasi-static manner to mimic the haemodynamics of progressive pressure overload as well as dynamically, where activation of each pocket allows recreation of the dynamics of a stenotic aortic valve. Notably, the dynamics and pressure levels of each pocket of the biomimetic sleeve can be independently controlled during both systole and diastole, enabling mimicry of a broad range of motion dynamics that could recapitulate those of the aortic valve of patients with AS.

Following *in vitro* and *in silico* characterization of the haemodynamics induced by sleeve actuation, we developed an *in vivo* model of AS. We leveraged MRI, echocardiography, and LV catheterization studies to demonstrate that our model can accurately recapitulate the haemodynamic derangements associated with mild, moderate, and severe cases of AS, which we validated using a broad spectrum of metrics used clinically for the diagnosis and staging of AS[31]. These included the iEOA, maximum and mean transaortic pressure gradient, peak jet flow velocity, ELI, and Z_{VA}. In addition, MRI studies enabled visualization of the blood flow velocity profiles along the aorta and at various cross-sectional planes at both the ascending and descending aorta as well as the aortic arch. Findings highlight that vorticity, and thus the TKE, increase even further for the bicommissural and unicommissural morphologies compared to the calcific tricuspid AS, in agreement with the clinical literature[39,40].

The enhanced control provided by our biomimetic soft robotic aortic sleeve could enable high-accuracy studies of pressure overload secondary to AS. Preclinical models of this condition are currently limited by poor control over the degree of aortic constriction and resulting haemodynamics as well as by elevated mortality rates. Chronically, AS may lead concentric remodelling and symptoms of heart failure with preserved ejection fraction (HFpEF)[16,43–45]. Further, depressed contractility and heart failure with reduced ejection fraction (HFrEF) may ensue in severe cases of AS when cardiac compensation is inadequate[46]. By enabling the recapitulation of patient-specific haemodynamics, this work could enable *in vivo* studies of the progression of heart failure secondary to AS, closely mimicking the pathophysiology of chronic disease and overcoming the limitations of existing models.

In addition, our sleeve enables controllable reversal of the degree of aortic constriction (or de-banding), and therefore has the potential to elucidate insights into the efficacy

of aortic valve replacement procedures in ameliorating adverse remodelling. This may enable evaluating early aortic valve replacement before the onset of irreversible myocardial dysfunction, in which standard of care relies heavily on echocardiography. Characterization of the onset of plasticity during these processes would also be enabled – specifically the point where pathophysiological remodelling cannot be fully reversed[47,48].

Patient-specific AS lesions and congenital valve defects lead to a dramatic acceleration in the progression of AS and associated symptomatology[25,27,29]. While *ex vivo* models of congenital valve disease have been recently developed[49], in this work, we have recreated the haemodynamics of bicommissural and unicommissural congenital defects as well as calcific AS *in vivo*. The ability of this bio-inspired soft robotic sleeve to be dynamically programmed and actuated, and reconfigured to various constriction profiles, makes it ideal for long-term studies of aortic constriction and congenital defects. Furthermore, we demonstrated that the design of the sleeve can be customized to match patient-specific morphologies of AS, which could lead to substantially more elevated haemodynamic mimicry compared to traditional aortic banding devices or techniques.

We have addressed several of the shortcomings of other AS and LV pressure overload models. However, future studies are warranted to further improve the clinical relevance of our proposed approach. First, the use of an extravascular sleeve may have important consequences on ventriculo-arterial coupling. By limiting the ability of the ascending aorta to expand in response to various haemodynamic states, stimuli, or regulatory mechanisms, the resistance and compliance of the aortic vessel may be severely impacted. Chronically, these changes may be exacerbated by any remodelling processes induced by elevations in aortic wall stress resulting from extravascular constriction. Additionally, implantation of the sleeve distally to the native aortic valve may have implications on coronary flow, which may affect chronic myocardial remodelling processes associated with AS and pressure overload. In the *in vivo* studies described in this work, we preserved the anatomy and function of the native aortic valve of the animals. Our *in vitro* and *in silico* studies suggest that some variations in flow patterns may arise from the presence of the native valve in series with the aortic sleeve. Therefore, additional investigations may be required to establish whether the accuracy of this model can be improved further. Finally, this model aims to recapitulate the biomechanics and haemodynamics of AS and LV pressure overload, and the recreation of the biological mechanisms involved in these processes goes beyond the scope of this work but is enabled by the current technological advances.

Outlook

We have described the development of high-fidelity, user-controllable *in vivo* models of human disease by leveraging soft robotics technology and advances in MRI. The models leverage haemodynamic mimicry and may facilitate the development of patient-specific applications. The models could also facilitate the clinical translation of treatments; in particular, a cohort of AS patients could be recapitulated in an *in vivo* porcine model, and new treatments could be evaluated preclinically. This work may also inspire *in vivo* models of other pathophysiological conditions, within and beyond the cardiovascular field. For example, the design of the aortic sleeve could be modified to enable studies of pulmonary

hypertension and right-heart failure, where flow patterns across the pulmonary valve can be accurately recreated. Other uses outside the cardiovascular space may involve studies of oesophageal and swallowing disorders, including abnormal peristalsis and spasms, and of the aerodynamics of airway obstructions for a variety of biomedical applications.

Methods

Mechanical characterization

The modulus of elasticity of the TPU and fabric layers was determined by uniaxial tensile loading using an electromechanical tester (Instron 5566, 2kN load cell, Norwood, USA), according to the ISO 527–1 and ISO 13934–1 standards for plastics and textiles respectively. The modulus was calculated as the slope of the stress-strain curve at 0–5% elongation.

The axial force exerted by the actuator at inflation was measured on the same instrument. The lower plate of the electromechanical tester served as an attachment point for the aortic sleeve. The upper plate was connected to the load cell and the height was adjusted until it was contacting the upper surface of the actuator. Under quasi-static conditions, the sleeve was actuated by deploying up to 5mL of saline using a syringe pump (70–3007 PHD ULTRA™ Syringe Pump Infuse/Withdraw, Harvard Apparatus) at a rate of 0.2 mL/sec, and the applied force was measured by the load cell. Dynamic actuation at a rate of 0.5 Hz was achieved from 2 psi to 14 psi in increments of 2 psi, as controlled by an in-house pressure control box. Actuation of the sleeve to each desired pressure level was followed by depressurization, with a 50% duty cycle and a period of 2 seconds.

Mock circulatory loop for haemodynamic studies

A MCL was built using a pulsatile pump (SuperPump, ViVitro Labs), an anatomically accurate compliant silicone aortic vessel (E ≈ 1 MPa, United Biologics) connected to two adjustable compliance chambers (i.e., ventricular, systemic), and a resistive valve. The modulus of the aortic vessel mimics that of the native human aorta (0.5 – 6MPa)[50,51]. The pulsatile pump was programmed to eject into a chamber causing contraction of a compliant LV (United Biologics) with a systolic time period equal to 34% of entire cardiac cycle. A Propylene Glycol (SK Picglobal) solution (40 v/v% in distilled water) of blood-mimicking viscosity 4.3 ± 0.8 mPa s (3.5 – 5.5 mPa s)[52] served as a surrogate fluid. The dynamic viscosity of the surrogate blood-mimicking fluid (4.3 ± 0.8 mPa s) was determined by a parallel plate rheometer setup (TA-65 Instruments, AR 2000) equipped with a 25-mm parallel plate probe (stainless steel). All measurements were performed at room temperature with probe oscillating at 10% strain and 1-Hz frequency maintained at a gap of 200 μm.

A pressure sensor (PRESS-S-000, PendoTech, Princeton, NJ) enabled LV pressure measurements, while a 5F pressure catheter (Ventri-Cath 510, Millar) connected to the MPVS Ultra acquisition system (Millar) was used to measure the pressure downstream of the sleeve (approximately 2 cm distal to the constriction plane). We monitored flow using a cardiac flow probe (ME 13 PXN, Transonic), and inserted an endoscopic camera (1080P HD, 30 fps, NIDAGE) to visualize the cross-sectional profiles of the aorta during actuation. The stroke volume and the rate of the pulsatile pump were manually adjusted

to maintain a cardiac output of 3.2 L/min. The soft robotic sleeve was secured around the aortic vessel and was actuated dynamically using our in-house pressure control box. The LV and aortic pressures, flow, and actuation pressures were displayed in real-time and recorded continuously (LabChart Pro v8.1.16, ADInstruments). We used the MATLAB (R2020a) Image Processing and Computer Vision toolbox (MathWorks®) to estimate the EOA from images of the luminal cross-sections recorded by the endoscopic camera. MATLAB (R2020a) was also used for processing and analysis of the haemodynamic data.

Mock circulatory loop for MRI studies

The MCL set-up was adapted for the magnetic resonance (MR) environment. Imaging was performed on a MAGNETOM Skyra (Siemens Healthineers, Erlangen, Germany) scanner. For MRI testing, all the ferromagnetic components of the MCL were replaced with plastic materials or kept outside of the MR room. The pulsatile pump (Harvard Apparatus) in the control room was connected to a Polyvinyl chloride (PVC) plastic tubing ($d_{in} = 3/4$", $d_{out} = 1$", McMaster-Carr). The compliance chambers, pressure sensors, and endoscopic camera were removed for safety in the MR environment, while a flow sensor (MA20PSB, Transonic) was attached downstream of the pulsatile pump as providing the triggering signal for dynamic actuation of the soft robotic sleeve on LabChart Pro (v8.1.16, ADInstruments). Actuation lines were used to connect the pressure control box located in the control room to the sleeve on the MR table. A solution of Gadolinium (0.07 v/v% in distilled water) was used in this experiment as the surrogate fluid to ensure sufficient signal for imaging.

We obtained cine and 4D flow MRI using analogous sequences as those defined for the animal studies (see *Magnetic resonance imaging* section below), at a resolution 0.67×0.67mm, and using a simulated ECG signal with an RR period selected to be equal to that of the pulsatile pump after performing real-time CINE acquisition to estimate the effective pulsatile period. The signal-to-noise ratio (SNR) of the phase contrast magnitude images was equal to 48.5 ± 9.9. This was computed by subtracting two symmetrically flow-encoded magnitude images with analogous magnitudes during the flow cycle over a 20×15mm region of interest in the centre of the image[53,54]. The SNR was therefore estimated using equation (1)[53]:

$$\text{SNR} = \frac{S\sqrt{2}}{SD} \tag{1}$$

where S is the signal, and noise is defined as the standard deviation (SD) of the subtracted image over the same ROI. The soft robotic sleeve was actuated in the presence and absence of an organic porcine valve (around 4 cm proximal to the sleeve) to investigate local haemodynamics changes in these two conditions. Multi-level thresholding was performing on MATLAB (R2020a, MathWorks®) to de-noise the *in vitro* MRI data prior to analysis.

FE modelling

FE modelling was conducted to evaluate the haemodynamic effects of actuations of the soft robotic sleeve. The heart model was adapted from the Living Heart Model (LHM) and used on Abaqus 2018 software (Abaqus 2018, SIMULIA™, Dassault Systèmes®). To simulate the cardiac cycle in a swine model, the LHM geometry was scaled down to approximate

in vivo measurements (global ratio~0.9, aortic arch ID~18mm, OD~19mm) and a nonlinear explicit dynamic analysis was performed. The FE model of the heart contained 208,561 linear tetrahedral elements and 47,323 nodes.

An accurate 3D representation of the sleeve was constructed in SOLIDWORKS (Dassault Systèmes, 2019) and imported into the FE model. The sleeve pockets were modelled as 3-node triangular shell elements (S3R) and assigned Neo-Hookean hyperelastic TPU material properties (Fig. 1d). The material characteristics prescribed to the ascending aorta ($E = 1$MPa, $\rho = 1070$ kg/m^3) were defined to mimic those of the silicone aortic model (UnitedBiologics) used in the *in vitro* set-up, and the damping capacity of arterial compliance was adjusted to recreate *in vitro* haemodynamics for cross-validation of the models. The LV was modelled using an anisotropic hyperelastic material formulation, and a time-varying elastance model was implemented to describe the active cardiac tissue mechanics[55]. Surface-based fluid cavities were defined to represent the fluid inside the actuator pockets, the aortic arch, and the ventricular chambers. Further details regarding the LHM can be found in previous studies[30,56].

The FE simulation consisted of two steps. In the first step, the pockets of the soft robotic sleeve were depressurized to achieve a deflated shape. In the second step, the sleeve was actuated dynamically and the cardiac cycle was simulated using the fluid cavity-based lumped parameter model. These studies were performed using the Abaqus/Explicit solver and were completed in approximately 8 hours on a desktop PC with a 3.0 GHZ i7–9700 processor with 8 cores and 32 GB RAM.

Animal preparation

All animal procedures were approved by the Institutional Animal Care and Use Committee (IACUC) of our institute. *In vivo* studies were conducted on 7 Yorkshire swine (~38–45kg) housed in the Massachusetts General Hospital Center for Comparative Medicine Large Animal Facility. Implantation of the aortic band involved a thoracotomy with incisions at the fourth intercostal space and blunt dissection. The sleeve was wrapped around the ascending aorta (approximately 1.2 cm distal to the native aortic valve), pre-tensioned, and then secured using sutures. Pre-tensioning was considered successful when the strip could be pulled entirely through the slit and no space between the sleeve and the porcine aorta could be noticed upon visual and tactile inspection. Due to anatomical variations, adequate pre-tensioning could not be achieved in two pigs, which were therefore discarded from the analysis.

Prior to the MRI study (D6), the animals were administered anaesthesia and intubated. Body temperature was supported using a circulating water heat pad. A finger pulse transducer (TN1012/ST Pulse Transducer DIN, ADInstruments), a blood pressure cuff and spirometer were placed to monitor the animals' vitals throughout the scanning procedures. Before terminal haemodynamic evaluation (D8), the swine were placed under anaesthesia. Echocardiography and LV catheterization enabled the characterization of LV and aortic haemodynamics under quasi-static and dynamic actuation. To achieve dynamic actuation, we used the pulse and the LV pressure signals to synchronize sleeve actuation with the native heartbeat of the swine during MRI and terminal haemodynamic evaluation,

respectively. The animals were then euthanized with saturated potassium chloride. Changes in the animal's heart rate and blood pressure due to anaesthesia were monitored.

Echocardiography

LV systolic function and flow profile across the proximal ascending aorta were evaluated using a commercial ultrasound system (IE33/X5–1 or X7–2 transducer, Philips, Andover, MA) at D0 (transthoracic) and at D8 (transepicardial). M-mode echocardiography on the LV in short axis view and continuous pulse-Doppler echocardiography across the proximal ascending aorta in an apical view were recorded during quasi-static or dynamic activation of the aortic sleeve to evaluate changes in the LV function and the flow profile due to aortic constriction[57]. Acquired echocardiographic data were analysed with syngo Dynamics software (Siemens Healthineers, Erlangen, Germany). From measurements of the LV end-diastolic and -systolic diameters, LV volumes and ejection fraction were estimated with the Teichholz method[58]. The mean transaortic pressure gradient ΔP_{mean} was calculated and the Peak pressure gradient ΔP_{max} was estimated from measured values of the peak outflow velocity v_{max} by the simplified Bernoulli equation[36] (equation (2)):

$$\Delta P_{max} = 4 \quad v_{max}^2 \tag{2}$$

Echocardiographic studies were conducted on n = 2 swine, as these procedures were included in the protocol only at a later stage.

In vivo Magnetic resonance imaging

Each animal was scanned one of two 3T clinical MRI systems (Biograph mMR scanner, 45mT/m gradient system and a MAGNETOM Prisma, 80mT/m gradient system, Siemens Healthineers, Erlangen, Germany), both equipped with a standard 32-channel antero-posterior surface coil. Animals were imaged with a whole heart CINE MRI as well as 2D/4D cardiac flow MRI sequences centred on the aortic constriction. Whole heart CINE MRI acquisitions were performed with a balanced steady-state free precession (bSSFP) sequence along the short axis plane with the following parameters: resolution 1.4×1.4×6.0 mm^3, matrix size 128/85, 10/15 slices depending on the heart size, pixel bandwidth (BW) 1500 Hz/pixel, echo time (TE) 2.79 ms, repetition time (TR) 30.72 ms, echo spacing 3.9 ms, and retrospective ECG gating with 25 segments. The aortic flow sequence was done with a 2D or 3D gradient echo (GRE) sequence depending on the scanner used.

On the Biograph mMR scanner, 2D flow was acquired with velocity encoding along the through-plane direction and images obtained in the short axis plane centred on the aortic band. The sequence parameters for the 2D flow were the following: velocity encoding (VENC) 500 cm/s, resolution 1.4×1.4×6.0 mm^3, matrix size 256×152 and 12 to 15 slices, BW 490 Hz/pixel, TE/TR 3.41/23.52 ms and retrospective ECG gating over 23 segments. On the MAGNETOM Prisma scanner, the 4D flow sequence was acquired with velocity encoding along the through-plane direction, left/right and head/feet directions and images obtained in the short axis plane centred on the aortic band. The sequence parameters were the following: velocity encoding (VENC) 500 cm/s, resolution 1.4×1.4×2.5 mm^3, matrix size 208×166 and 28 slices to cover the entire aortic arch, BW 490 Hz/pixel, TE/TR

2.07/15.6 ms, retrospective ECG gating over 27 segments and respiratory gating with a pencil beam navigator placed on the liver dome and acceptance window of 8mm.

LV catheterization

In vivo LV PV data were collected using the Transonic ADV500 PV System and the 5F straight tip PV loop catheter (Transonic Systems, Inc., Ithaca, NY). The catheter was inserted transapically during the open-chest surgery. Through real-time pressure measurements, the catheter was guided through the aortic valve and gradually retrack back to the LV to ensure consistent catheter positioning. The catheter was then rotated to minimize the interference with mitral-valve and/or papillary muscle. Data were collected with 400 Hz sampling rate and a 50 Hz low-pass filter was applied to the volume data.

Evaluation of clinical parameters

Clinical metrics used in this work for the evaluation of the severity of AS in our *in vivo* model include the iEOA, P_{max}, P_{mean}, v_{max}, ELI, and Z_{VA}.

iEOA is calculated using the Gorlin equation[31] (equation (3)):

$$iEOA = \frac{Q}{BSA \ 51.6 \ \sqrt{\Delta P_{mean}}} \tag{3}$$

where Q is the flow through the aortic valve and was measured from the PV catheter, BSA is the body surface area of the animal, and P_{mean} is the mean pressure gradient. In this study, the PV catheter was maintained in the LV during actuation of the sleeve. Therefore, P_{mean} estimates from echocardiography (not from LV catheterization) were used in equation (3).

P_{mean} and v_{max} were obtained directly from echocardiography, whereas P_{max} was estimated from measurements of v_{max} (see Echocardiography section above).

ELI was estimated using equation (4)[59]:

$$ELI = \frac{EOA \ (A_a)}{BSA(A_a - EOA)} \tag{4}$$

where EOA is the absolute effective orifice area, and Aa is the cross-sectional area of the aorta measured at the sinotubular junction (as measured with MRI).

Finally, Z_{VA} was measured using equation (5)[60]:

$$Z_{VA} = \frac{LVP_{max}}{SV}BSA \tag{5}$$

where LVP_{max} is the peak systolic LV pressure and SV is the stroke volume (SV). Both parameters were obtained from LV catheterization.

In equations (3–5), BSA (in m^2) was estimated from the body weight (BW) (in kg) of the swine using the Kelley formula[61] (equation (6)):

$$BSA = 0.0734 \quad BW^{0.656} \tag{6}$$

Patient-specific sleeve design and analysis

CT patient's data were obtained retrospectively via IRB approval at the Massachusetts General Hospital and anonymized. CT images of the aortic valve during systole were processed on Mimics Research (v.21.0.0.406, Materialise NV). We performed segmentation by thresholding, multiple-slice editing and auto-interpolation. A drawing exchange format (.dxf) 2D image of the patient's valve was then imported into SOLIDWORKS (Dassault Systèmes, 2019) and smoothed to create the patient-specific AS morphology. The closed contour of the leaflet was offset by the aortic wall thickness (1.3 mm), and the resulting geometry was unwrapped onto a plane to create the shape of the TPU expandable element of the patient-specific sleeve. The sleeve was then manufactured using the same methods as described for the non-specific sleeve, with the exception that only one actuation line was incorporated, instead of three.

We performed testing of the patient-specific sleeve on the MCL and recorded cross-sectional images of the mock aorta during dynamic actuation (8 psi) by means of the endoscopic camera. A similar procedure was repeated for a commercial aortic banding cuff (In Vivo Metric Systems, Healdsburg, CA), and for the non-specific sleeve. Images of the aortic cross-section recorded in the MCL were binarized and cross-registered with the patient-specific AS morphology, used as the fixed image on MATLAB (R2020a, MathWorks®). The *rigid* distortion option, i.e., enabling only translation and rotation of the moving image, was used for image registration, and the DSC was calculated for each condition.

Extended Data
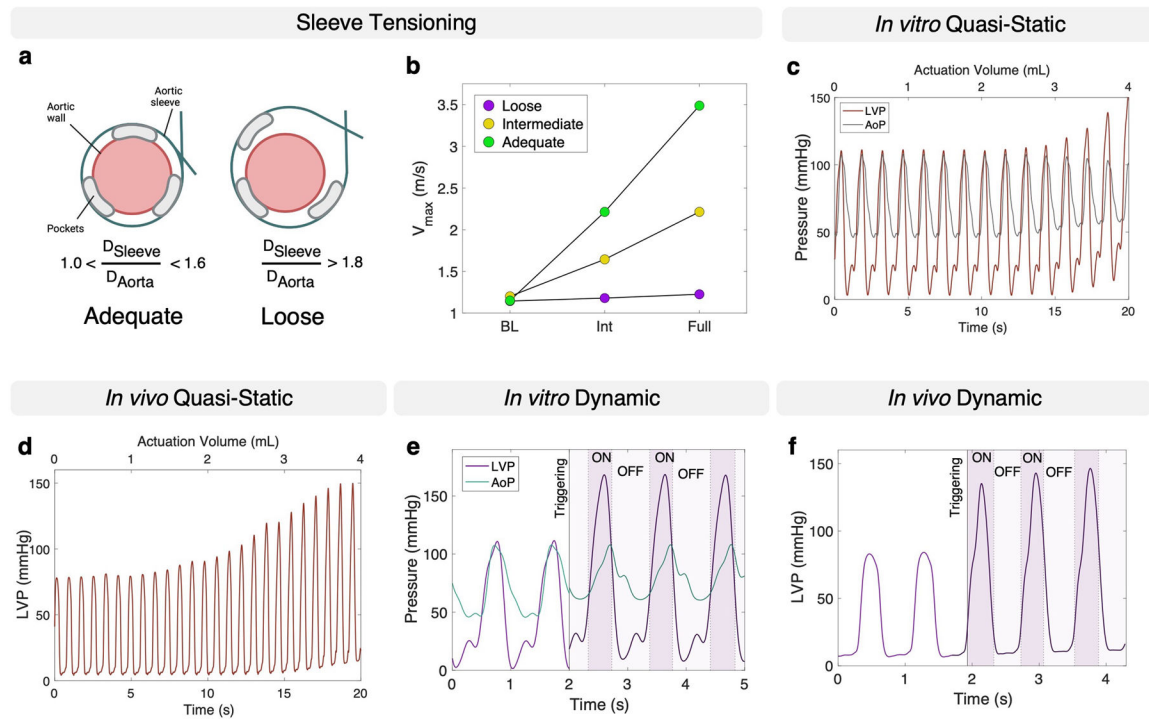
ED Fig. 1. Sleeve tensioning and representative hemodynamic data *in vitro* and *in silico* under quasi-static and dynamic conditions.

a, Illustration of an adequately and loosely implanted sleeve, showing the sleeve-to-aorta diameter ratio for classification. Ratios smaller than 1 would result in over-tensioning, and thus in aortic pre-constriction. Ratios greater than 1.8 would cause under-tensioning. **b,** Representative *in vivo* peak aortic flow velocity on MRI at baseline (BL), intermediate (Int: 3 mL), and full (4 mL) constrictions for the loose, intermediate, and adequately-pretensioned sleeve. **c,** Representative *in vitro* LVP and AoP under quasi-static actuation conditions. **d,** Representative LVP tracing *in vivo* measured under quasi-static actuation conditions. **e,** Representative LVP and AoP tracings *in vitro* with dynamic actuation. **f,** Representative LVP tracing *in vivo* with dynamic actuation. The ON and OFF marks indicate the intervals during which the sleeve was inflated or deflated respectively, following the start of the triggering.
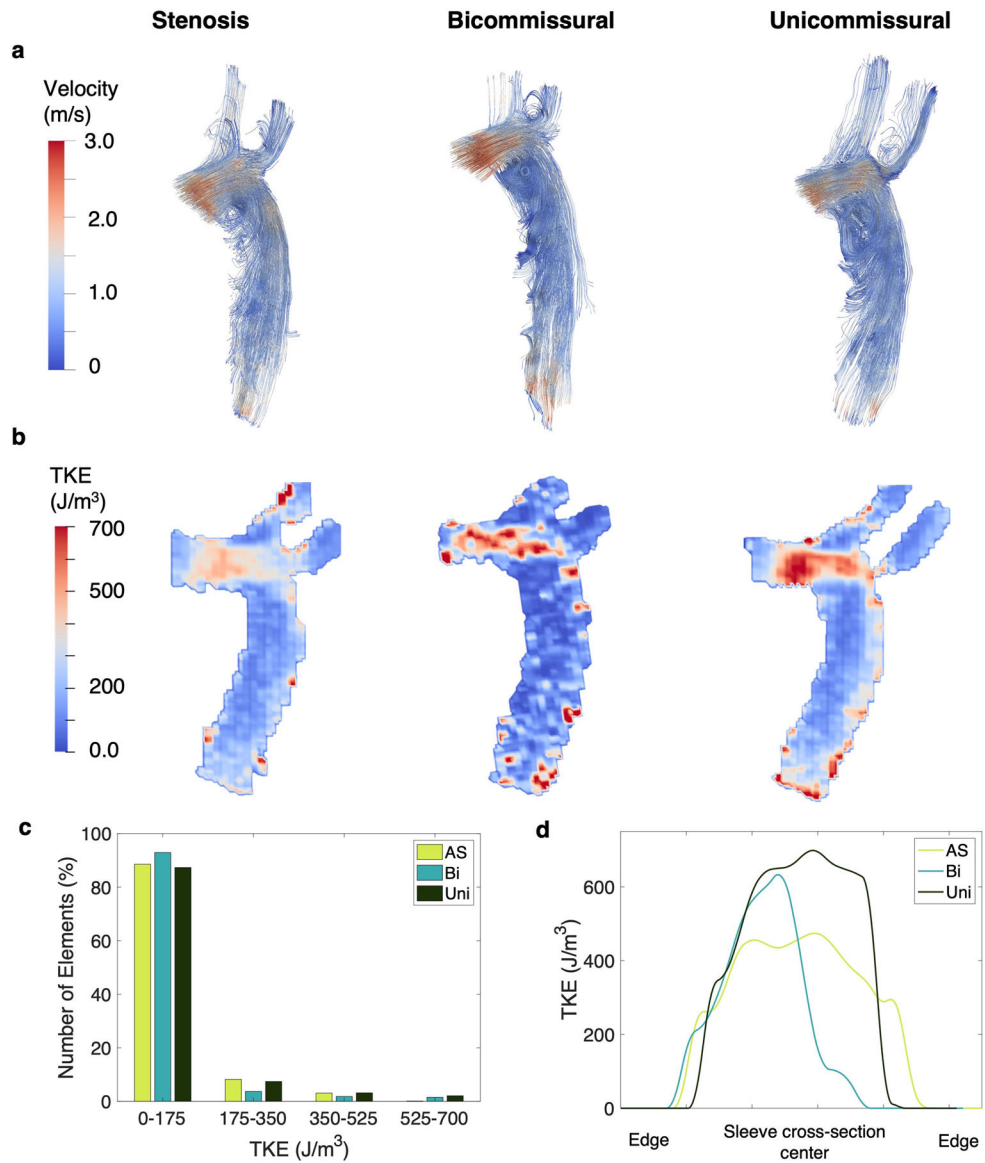
ED Fig. 2. *In vivo* **MRI aortic flow streamlines and turbulence kinetic energy (TKE).**
a, Aortic flow streamlines for the stenosis (AS), bicommissural (Bi), and unicommissural (Uni) constriction profiles. **b,** TKE map of the aorta of a longitudinal cross-section of the aorta and for the same constriction profiles. **c,** Distribution of elements across ranges of TKE within the aortic domain. **d,** TKE line plots along an aortic diameter at the sleeve plane.
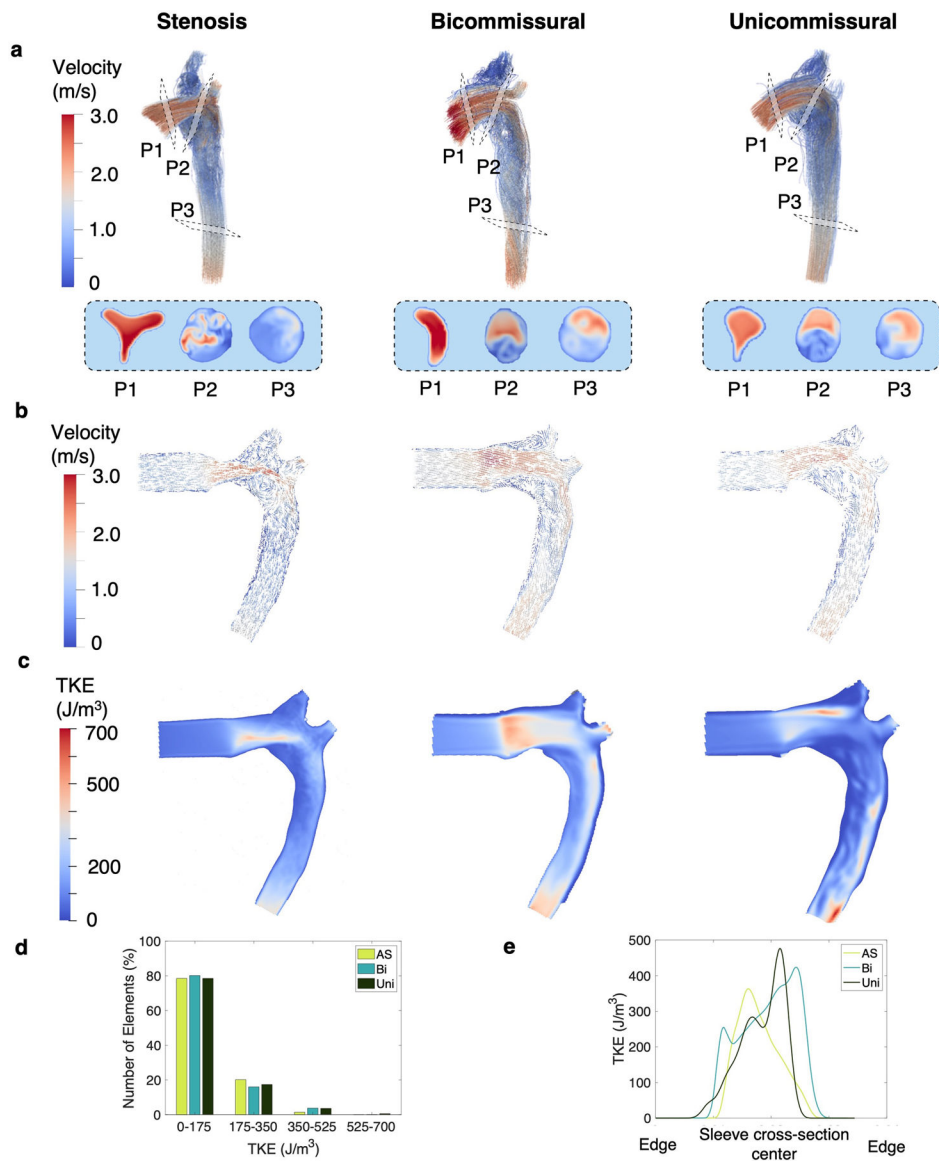
ED Fig. 3. CFD hemodynamics and TKE.
a, Aortic flow streamlines for the stenosis, bicommissural, and unicommissural constriction profiles, with details of transverse planes at the ascending aorta (P1), aortic arch (P2), and descending aorta (P3). **b,** 2D velocity vector maps of a longitudinal cross-section of the aorta for the three constriction profiles. **c,** TKE map of the same longitudinal cross-section for the three constriction profiles. **d,** Distribution of elements across ranges of TKE within the aortic CFD domain. **e,** TKE line plots along an aortic diameter at the sleeve plane.
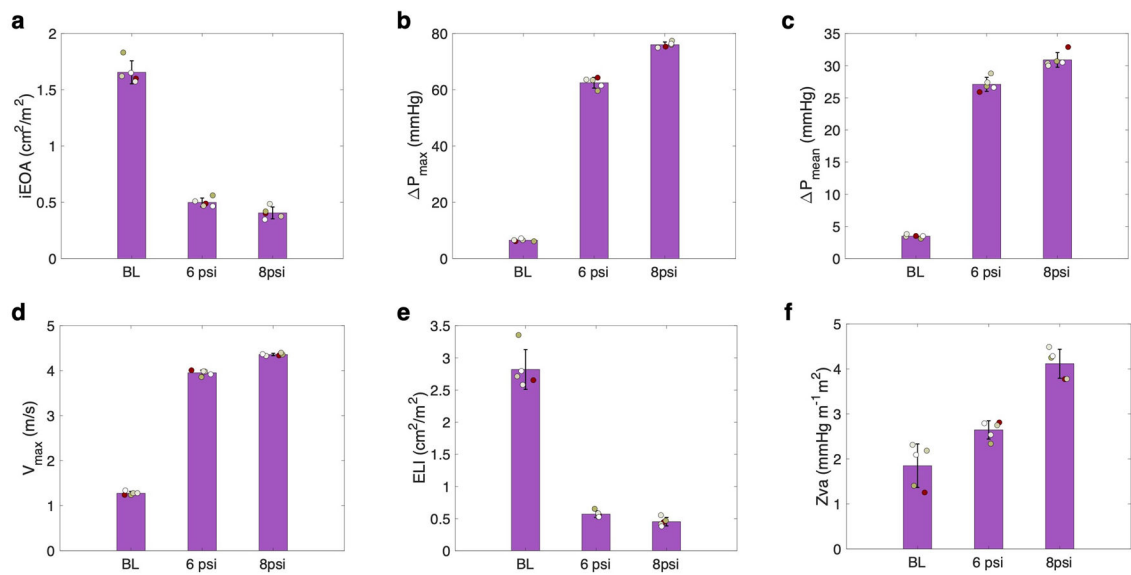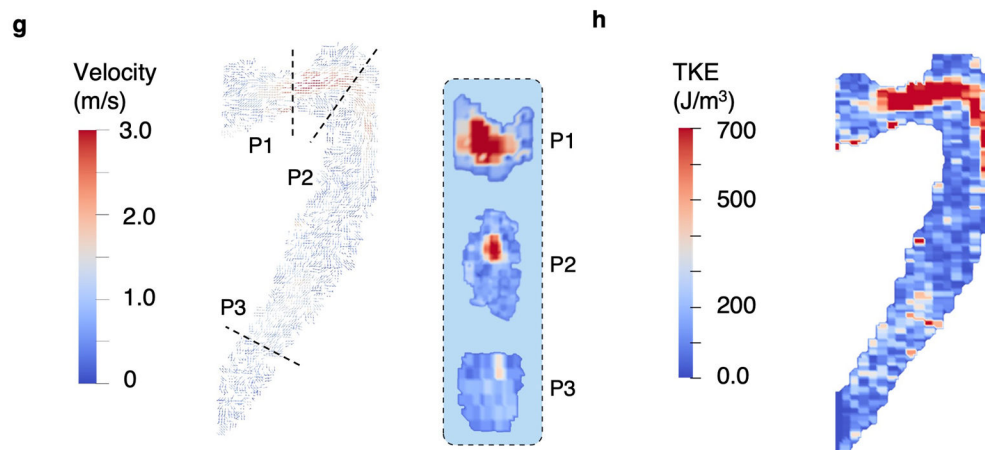
ED Fig. 4. *In vivo* **hemodynamic studies under dynamic actuation.**
a-f, Clinical metrics of AS obtained via echocardiography and LV catheterization. These include the **(a)** iEOA, **(b)** P_{max}, **(c)** P_{mean}, **(d)** v_{max}, **(e)** ELI, **(f)** Z_{VA}. Error bars, s.d., n = 5 for each data point, with 5 consecutive measurements taken for 1 animal. **g**, 2D velocity vector maps of the aorta with corresponding flow cross-sectional planes at the ascending aorta (P1), aortic arch (P2), and descending aorta (P3). **h**, Corresponding TKE map of the aorta.
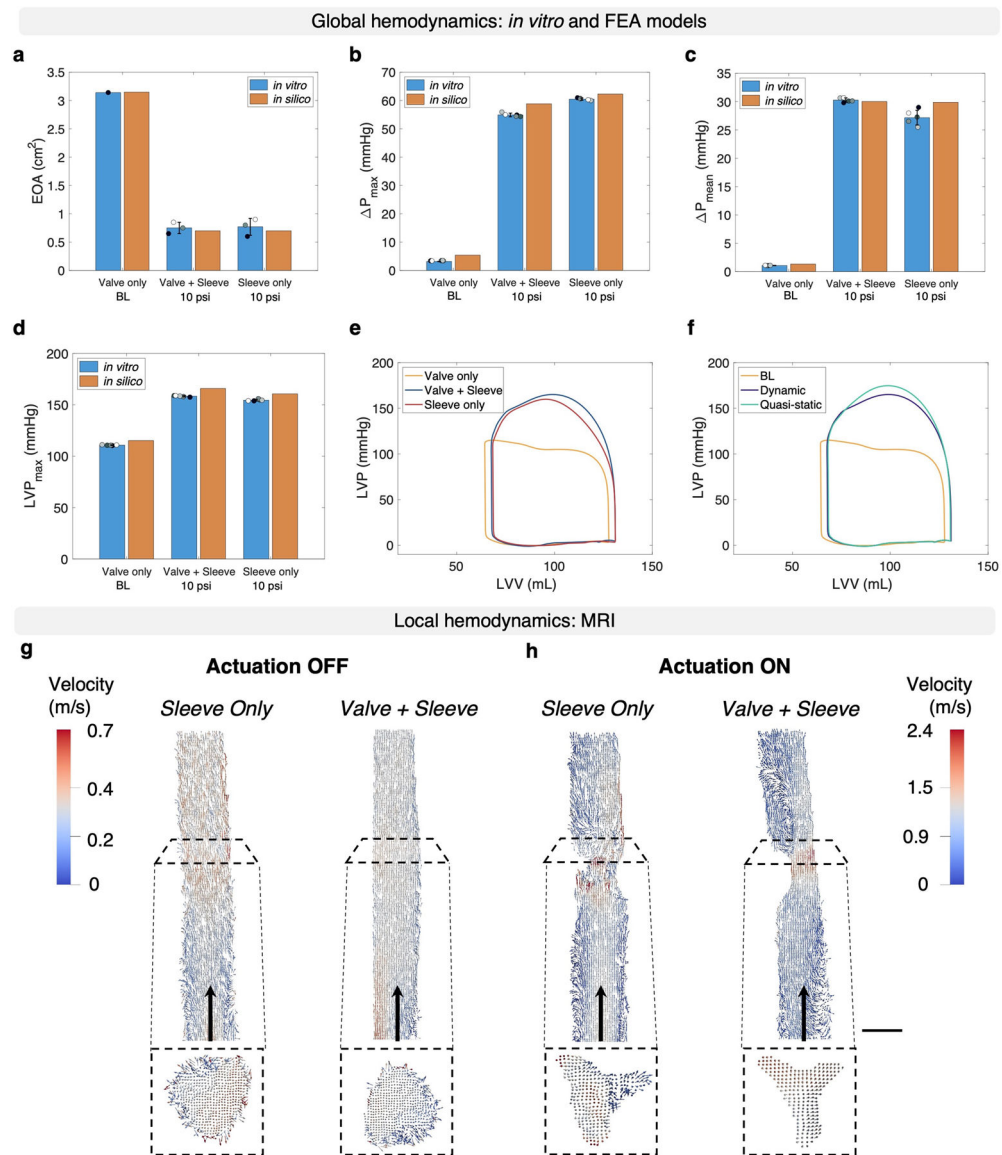
ED Fig. 5. Global and local hemodynamics in the presence or absence of a healthy valve in series with the aortic sleeve *in vitro*.
(a) EOA, (b) P_{max}, (c) P_{mean}, (d) LVP_{max} calculated at baseline (valve only; BL) and at 8 psi under dynamic actuation with (valve + sleeve) and without (sleeve only) a valve proximal to the sleeve. Error bars, s.d., n = 15 actuation cycles for each data point. **e,** LV PV loops at BL and 10 psi for the same groups. **f,** LV PV loops at BL, and for quasi-static and dynamic actuation. **g-h,** Longitudinal and cross-sectional 2D velocity vectors **(g)** before and **(h)** during actuation of the soft robotic aortic sleeve (sleeve only) and during actuation with a porcine valve inserted proximally to the sleeve (valve + sleeve). Results illustrate the cross-sectional geometry of the mock aortic vessel at the sleeve plane both prior to and during actuation for the two groups (sleeve only and valve + sleeve). Arrows indicate the direction of flow. Scale bar, 1.0 cm.

Supplementary Material

Refer to Web version on PubMed Central for supplementary material.

Acknowledgements

Data availability

All data supporting the findings of this study are available within the article and the Supplementary Information. Source data are provided with this paper. The raw and analysed data generated during the study are available from the corresponding authors on reasonable request.

References

1. Maglio S, Park C, Tognarelli S, Menciassi A & Roche ET High-Fidelity Physical Organ Simulators: From Artificial to Bio-Hybrid Solutions. IEEE Trans. Med. Robot. Bionics 3, 349–361 (2021).

2. Park C et al. An organosynthetic dynamic heart model with enhanced biomimicry guided by cardiac diffusion tensor imaging. Sci. Robot 5, eaay9106 (2020). [PubMed: 33022595]

3. Bhattacharya D, Ali SJV, Cheng LK & Xu W RoSE: A Robotic Soft Esophagus for Endoprosthetic Stent Testing. Soft Robot 8, 397–415 (2021). [PubMed: 32758017]

4. Dang Y et al. SoGut: A Soft Robotic Gastric Simulator. Soft Robot 8, 273–283 (2021). [PubMed: 32559391]

5. Ranunkel O, Güder F & Arora H Soft Robotic Surrogate Lung. ACS Appl. Bio Mater 2, 1490–1497 (2019).

6. Horvath MA et al. An organosynthetic soft robotic respiratory simulator. APL Bioeng 4, 026108 (2020). [PubMed: 32566890]

7. Lu X, Xu W & Li X A Soft Robotic Tongue—Mechatronic Design and Surface Reconstruction. IEEE/ASME Trans. Mechatronics 22, 2102–2110 (2017).

8. Horvath MA et al. Design and Fabrication of a Biomimetic Circulatory Simulator with Overlaid Flow and Respiration Mechanism for Single Ventricle Physiology in 2020 8th IEEE RAS/EMBS International Conference for Biomedical Robotics and Biomechatronics (BioRob) vols 2020-Novem, 74–79 (IEEE, 2020).

9. Nkomo VT et al. Burden of valvular heart diseases: a population-based study. Lancet 368, 1005–1011 (2006). [PubMed: 16980116]

10. Mrsic Z, Hopkins SP, Antevil JL & Mullenix PS Valvular Heart Disease. Prim. Care Clin. Off. Pract 45, 81–94 (2018).

11. Carabello BA & Paulus WJ Aortic stenosis. Lancet 373, 956–966 (2009). [PubMed: 19232707]

12. Bonow RO & Greenland P Population-Wide Trends in Aortic Stenosis Incidence and Outcomes. Circulation 131, 969–971 (2015). [PubMed: 25691712]

13. Coffey S et al. Global epidemiology of valvular heart disease. Nat. Rev. Cardiol 18, 853–864 (2021). [PubMed: 34172950]

14. Grossman W, Jones D & McLaurin LP Wall stress and patterns of hypertrophy in the human left ventricle. J. Clin. Invest 56, 56–64 (1975). [PubMed: 124746]

15. Borlaug BA & Paulus WJ Heart failure with preserved ejection fraction: pathophysiology, diagnosis, and treatment. Eur. Heart J 32, 670–679 (2011). [PubMed: 21138935]

16. Borlaug BA Evaluation and management of heart failure with preserved ejection fraction. Nat. Rev. Cardiol 17, 559–573 (2020). [PubMed: 32231333]

17. Taniguchi T et al. Sudden Death in Patients With Severe Aortic Stenosis: Observations From the CURRENT AS Registry. J. Am. Heart Assoc 7, e008397 (2018). [PubMed: 29776957]

18. Otto CM et al. 2020 ACC/AHA Guideline for the Management of Patients With Valvular Heart Disease: A Report of the American College of Cardiology/American Heart Association Joint Committee on Clinical Practice Guidelines. Circulation 143, e72–e227 (2021). [PubMed: 33332150]

19. Brennan JM et al. Long-Term Survival After Aortic Valve Replacement Among High-Risk Elderly Patients in the United States. Circulation 126, 1621–1629 (2012). [PubMed: 22907936]

20. Jones JM et al. Repeat heart valve surgery: Risk factors for operative mortality. J. Thorac. Cardiovasc. Surg 122, 913–918 (2001). [PubMed: 11689796]

21. Yarbrough WM et al. Progressive induction of left ventricular pressure overload in a large animal model elicits myocardial remodeling and a unique matrix signature. J. Thorac. Cardiovasc. Surg 143, 215–223 (2012). [PubMed: 22056365]

22. Olver TD et al. Western Diet-Fed, Aortic-Banded Ossabaw Swine. JACC Basic to Transl. Sci 4, 404–421 (2019).

23. Torres WM et al. Changes in Myocardial Microstructure and Mechanics With Progressive Left Ventricular Pressure Overload. JACC Basic to Transl. Sci 5, 463–480 (2020).

24. Singh GK Congenital Aortic Valve Stenosis. Children 6, 69 (2019).

25. Roberts WC & Ko JM Frequency by Decades of Unicuspid, Bicuspid, and Tricuspid Aortic Valves in Adults Having Isolated Aortic Valve Replacement for Aortic Stenosis, With or Without Associated Aortic Regurgitation. Circulation 111, 920–925 (2005). [PubMed: 15710758]

26. O'Brien KD Epidemiology and Genetics of Calcific Aortic Valve Disease. J. Investig. Med 55, 284–291 (2007).

27. Brantley HP, Nekkanti R, Anderson CA & Kypson AP Three-Dimensional Echocardiographic Features of Unicuspid Aortic Valve Stenosis Correlate with Surgical Findings. Echocardiography 29, E204–E207 (2012). [PubMed: 22676160]

28. Moller JH, Nakib A, Eliot RS & Edwards JE Symptomatic congenital aortic stenosis in the first year of life. J. Pediatr 69, 728–734 (1966). [PubMed: 5928004]

29. Singh S et al. Unicuspid Unicommissural Aortic Valve: An Extremely Rare Congenital Anomaly. Texas Hear. Inst. J 42, 273–276 (2015).

30. Baillargeon B, Rebelo N, Fox DD, Taylor RL & Kuhl E The Living Heart Project: A robust and integrative simulator for human heart function. Eur. J. Mech. - A/Solids 48, 38–47 (2014).

31. Saikrishnan N, Kumar G, Sawaya FJ, Lerakis S & Yoganathan AP Accurate Assessment of Aortic Stenosis. Circulation 129, 244–253 (2014). [PubMed: 24421359]

32. Rajani R, Hancock J & Chambers JB The art of assessing aortic stenosis. Heart 98, iv14–iv22 (2012). [PubMed: 23143121]

33. Borlaug BA The pathophysiology of heart failure with preserved ejection fraction. Nat. Rev. Cardiol 11, 507–515 (2014). [PubMed: 24958077]

34. Rosalia L, Ozturk C, Van Story D, Horvath MA & Roche ET Object-Oriented Lumped-Parameter Modeling of the Cardiovascular System for Physiological and Pathophysiological Conditions. Adv. Theory Simulations 4, 2000216 (2021).

35. Rosalia L, Ozturk C & Roche ET Lumped-Parameter and Finite Element Modeling of Heart Failure with Preserved Ejection Fraction. J. Vis. Exp 2021, e62167 (2021).

36. Baumgartner H et al. Recommendations on the echocardiographic assessment of aortic valve stenosis: a focused update from the European Association of Cardiovascular Imaging and the American Society of Echocardiography. Eur. Hear. J. - Cardiovasc. Imaging 18, 254–275 (2017).

37. Bahlmann E et al. Prognostic Value of Energy Loss Index in Asymptomatic Aortic Stenosis. Circulation 127, 1149–1156 (2013). [PubMed: 23357717]

38. Hachicha Z, Dumesnil JG & Pibarot P Usefulness of the Valvuloarterial Impedance to Predict Adverse Outcome in Asymptomatic Aortic Stenosis. J. Am. Coll. Cardiol 54, 1003–1011 (2009). [PubMed: 19729117]

39. Dyverfeldt P, Hope MD, Tseng EE & Saloner D Magnetic Resonance Measurement of Turbulent Kinetic Energy for the Estimation of Irreversible Pressure Loss in Aortic Stenosis. JACC Cardiovasc. Imaging 6, 64–71 (2013). [PubMed: 23328563]

40. Binter C et al. Turbulent Kinetic Energy Assessed by Multipoint 4-Dimensional Flow Magnetic Resonance Imaging Provides Additional Information Relative to Echocardiography for the Determination of Aortic Stenosis Severity. Circ. Cardiovasc. Imaging 10, e005486 (2017). [PubMed: 28611119]

41. Dice LR Measures of the Amount of Ecologic Association Between Species. Ecology 26, 297–302 (1945).

42. Iung B A prospective survey of patients with valvular heart disease in Europe: The Euro Heart Survey on Valvular Heart Disease. Eur. Heart J 24, 1231–1243 (2003). [PubMed: 12831818]

43. Mishra S & Kass DA Cellular and molecular pathobiology of heart failure with preserved ejection fraction. Nat. Rev. Cardiol 18, 400–423 (2021). [PubMed: 33432192]

44. Rosalia L et al. Device-Based Solutions to Improve Cardiac Physiology and Hemodynamics in Heart Failure With Preserved Ejection Fraction. JACC Basic to Transl. Sci 6, 772–795 (2021).

45. Rosalia L, Saeed Y, M. & Roche ET. Devices that Enhance the Biomechanics of the Failing Heart. in Advances in Cardiovascular Technology (eds. Karimov JH, Fukamachi K & Gillinov MBT-A in C. T.) 625–640 (Elsevier, 2022). doi:10.1016/B978-0-12-816861-5.00015-0.

46. Pibarot P et al. Moderate Aortic Stenosis and Heart Failure With Reduced Ejection Fraction. JACC Cardiovasc. Imaging 12, 172–184 (2019). [PubMed: 30621989]

47. Azevedo CF et al. Prognostic significance of myocardial fibrosis quantification by histopathology and magnetic resonance imaging in patients with severe aortic valve disease. J. Am. Coll. Cardiol 56, 278–287 (2010). [PubMed: 20633819]

48. Goldsmith EC, Bradshaw AD & Spinale FG Cellular Mechanisms of Tissue Fibrosis. 2. Contributory pathways leading to myocardial fibrosis: moving beyond collagen expression. Am. J. Physiol. Physiol 304, C393–C402 (2013).

49. Zhu Y et al. Novel bicuspid aortic valve model with aortic regurgitation for hemodynamic status analysis using an ex vivo simulator. J. Thorac. Cardiovasc. Surg 163, e161–e171 (2022). [PubMed: 32747120]

50. Gao F, Guo Z, Sakamoto M & Matsuzawa T Fluid-structure Interaction within a Layered Aortic Arch Model. J. Biol. Phys 32, 435–454 (2007).

51. Shirakawa T et al. Towards a Clinical Implementation of Measuring the Elastic Modulus of the Aorta From Cardiac Computed Tomography Images. IEEE Trans. Biomed. Eng 68, 3543–3553 (2021). [PubMed: 33945468]

52. Nader E et al. Blood Rheology: Key Parameters, Impact on Blood Flow, Role in Sickle Cell Disease and Effects of Exercise. Front. Physiol 10, 1329 (2019). [PubMed: 31749708]

53. Price RR et al. Quality assurance methods and phantoms for magnetic resonance imaging: Report of AAPM nuclear magnetic resonance Task Group No. 1. Med. Phys 17, 287–295 (1990). [PubMed: 2333055]

54. van Ooij P et al. Wall shear stress estimated with phase contrast MRI in an in vitro and in vivo intracranial aneurysm. J. Magn. Reson. Imaging 38, 876–884 (2013). [PubMed: 23417769]

55. Guccione JM & McCulloch AD Mechanics of Active Contraction in Cardiac Muscle: Part I—Constitutive Relations for Fiber Stress That Describe Deactivation. J. Biomech. Eng 115, 72–81 (1993). [PubMed: 8445901]

56. Genet M, Lee LC, Baillargeon B, Guccione JM & Kuhl E Modeling Pathologies of Diastolic and Systolic Heart Failure. Ann. Biomed. Eng 44, 112–127 (2016). [PubMed: 26043672]

57. Mitchell C et al. Guidelines for Performing a Comprehensive Transthoracic Echocardiographic Examination in Adults: Recommendations from the American Society of Echocardiography. J. Am. Soc. Echocardiogr 32, 1–64 (2019). [PubMed: 30282592]

58. Stypmann J et al. Echocardiographic assessment of global left ventricular function in mice. Lab. Anim 43, 127–137 (2009). [PubMed: 19237453]

59. Pibarot P, Garcia D & Dumesnil JG Energy Loss Index in Aortic Stenosis. Circulation 127, 1101–1104 (2013). [PubMed: 23479666]

60. Nuis R-J et al. Impact of Valvulo-Arterial Impedance on Long-Term Quality of Life and Exercise Performance After Transcatheter Aortic Valve Replacement. Circ. Cardiovasc. Interv 13, e008372 (2020). [PubMed: 31937136]

61. Itoh T et al. Body surface area measurement in juvenile miniature pigs using a computed tomography scanner. Exp. Anim 66, 229–233 (2017). [PubMed: 28367864]
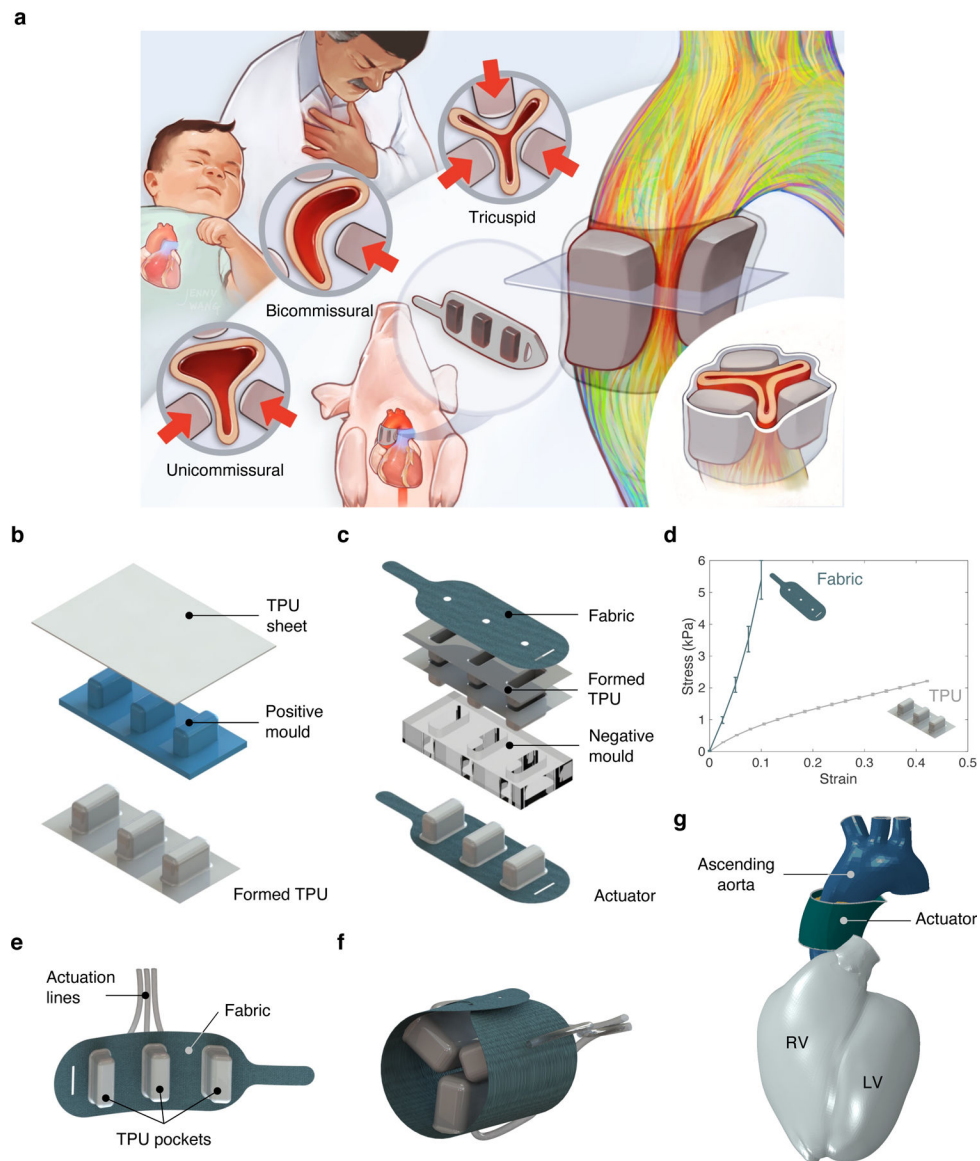
**Fig. 1 |. Concept and design of the soft robotic aortic sleeve.**

a, High-fidelity *in vivo* model of AS based on a biomimetic soft robotic aortic sleeve. The tunability of the sleeve enables the recreation of the haemodynamics of AS and of congenital valve abnormalities, including those of bicommissural and unicommissural aortic valves. **b**, Two TPU sheets are vacuum formed to a 3D-printed mould. **c**, The two TPU sheets are heat-sealed together creating three distinct expandable pockets, which are then attached to a strain-limiting fabric thorough a heat-sealing process that uses a negative of the 3D-printed mould. **d**, Stress-strain response of the TPU and fabric layers under uniaxial tension. Error bars, s.d., n = 3 for each data point. **e**-**f**, 3D views of the aortic sleeve with details of the individual TPU pockets, constraining fabric, and hydraulic lines for actuation. **g**, FE model illustration including a 3D representation of the soft robotic sleeve on the ascending aorta. RV, right ventricle.
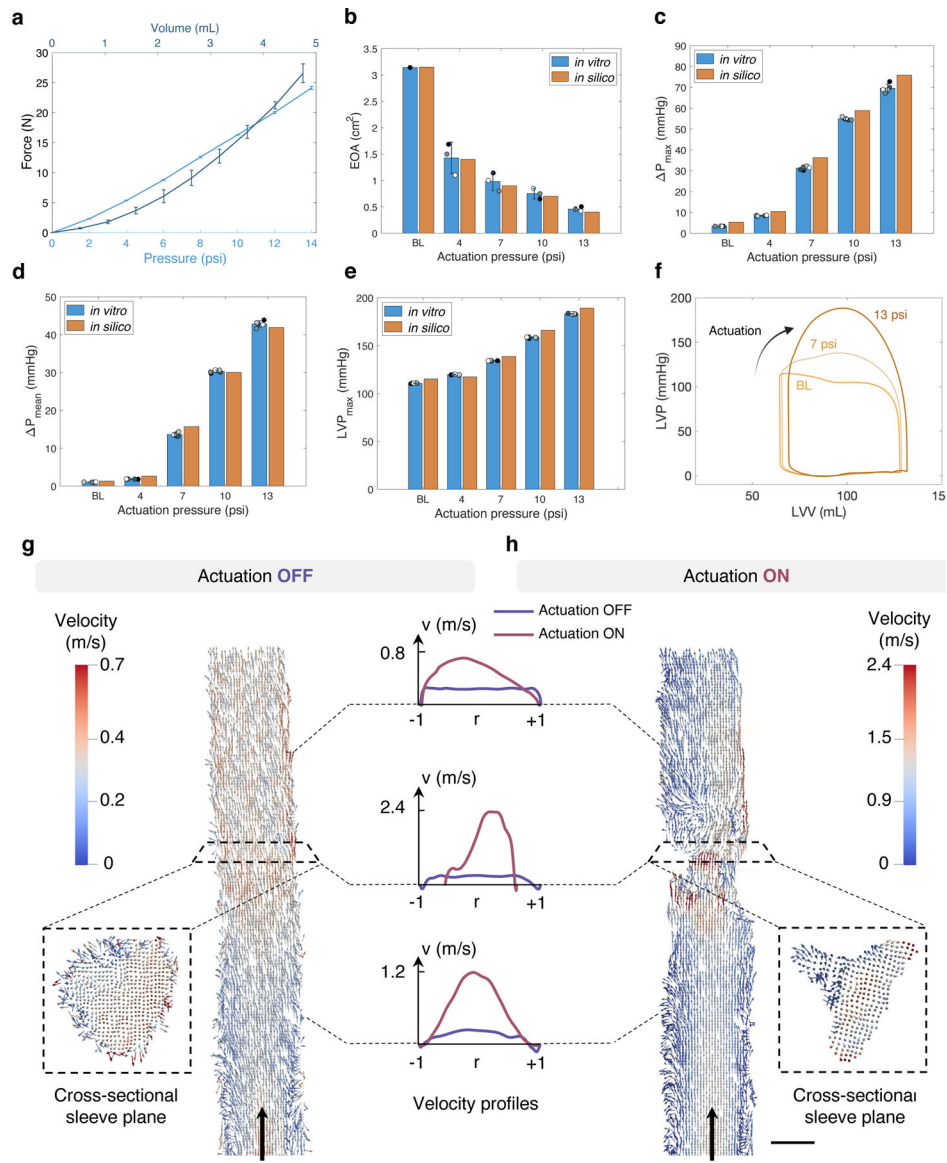
Fig. 2 |. *In vitro* and *in silico* **characterization of the biomimetic soft robotic aortic sleeve.**
a, Axial force exerted by the bioinspired soft robotic aortic sleeve versus actuation volume and pressure. Error bars, s.d., n = 3 for each data point. **b-d,** Global haemodynamics predicted *in vitro* and *in silico* at baseline (BL) and at various actuation pressures, including **(b)** EOA (n = 3), **(c)** P_{max}, **(d)** P_{mean}, and **(e)** LVP_{max}. **f,** Representative PV loops obtained *in silico*. LVV: left ventricular volume. **(c-e)** Error bars, s.d., n = 5 actuation cycles for each data point. **g-h,** Longitudinal and cross-sectional 2D velocity vectors **(g)** before and **(h)** during dynamic actuation of the soft robotic aortic sleeve. Results illustrate the velocity magnitudes from −1 to +1 *r* (radius) at the sleeve plane, as well as upstream and downstream of the sleeve plane and the cross-sectional geometry of the mock aortic vessel at the sleeve plane both prior to and during actuation. Arrows indicate the direction of flow. Scale bar, 1.0 cm.
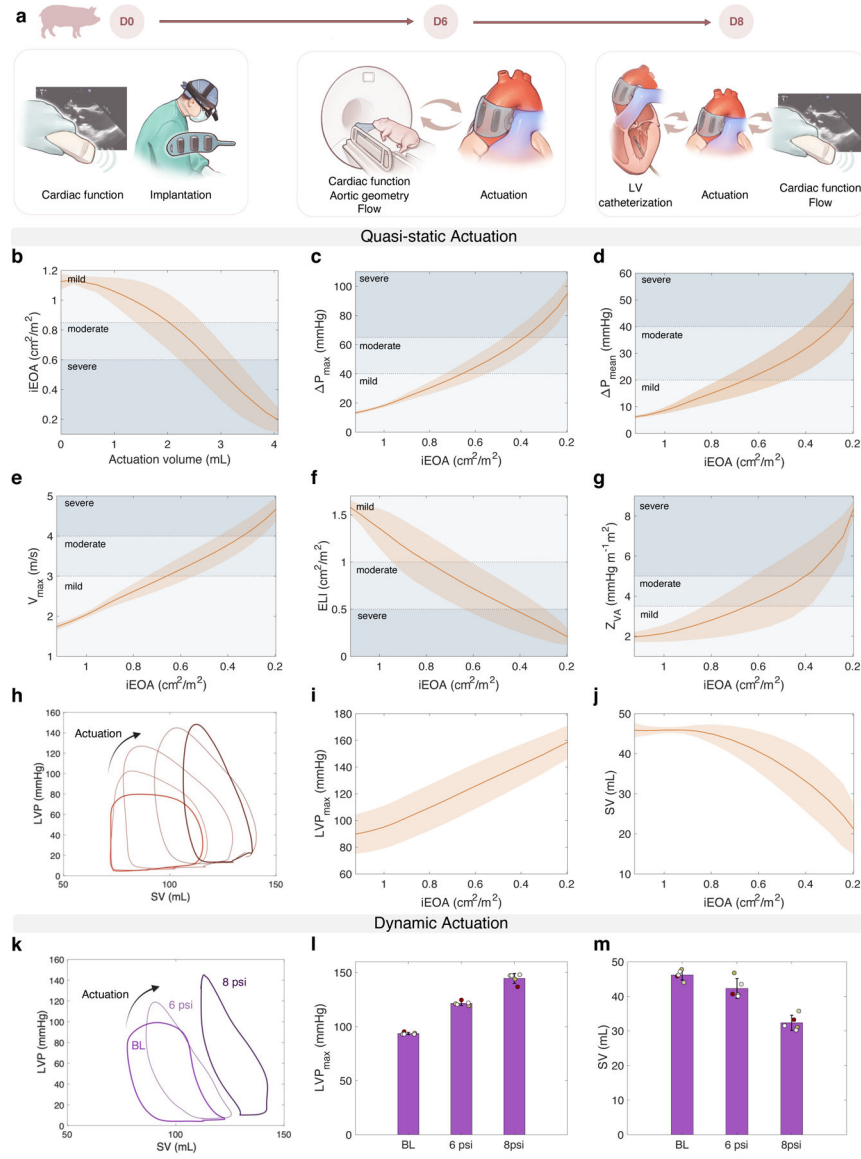
Fig. 3 |. *In vivo* **haemodynamics of quasi-static and dynamic aortic constriction.**
a, Timeline of *in vivo* study, with TTE prior to sleeve implantation (D0), MRI studies six days post-surgery (D6), and LV catheterization and transepicardial echocardiography eight days after implantation (D8). **b-j** *In vivo* global haemodynamics under quasi-static actuation, with indications of relative clinical thresholds for staging of AS. Metrics include **(b)** iEOA, **(c)** ΔP_{max}, **(d)** ΔP_{mean}, **(e)** v_{max}, **(f)** ELI, **(g)** Z_{VA}, **(h)** LV PV loops, **(i)** LVP$_{max}$, and **(j)** SV. Shaded area, s.d., n = 6 for each data point, with 3 consecutive measurements taken for 2 animals. **k-m** *In vivo* global haemodynamics under dynamic actuation at BL and two actuation pressures, including **(k)** representative PV loops, **(l)** LVP$_{max}$, and **(m)** SV. Error bars, s.d., n = 5 for each data point, with 5 consecutive measurements taken for 1 animal.
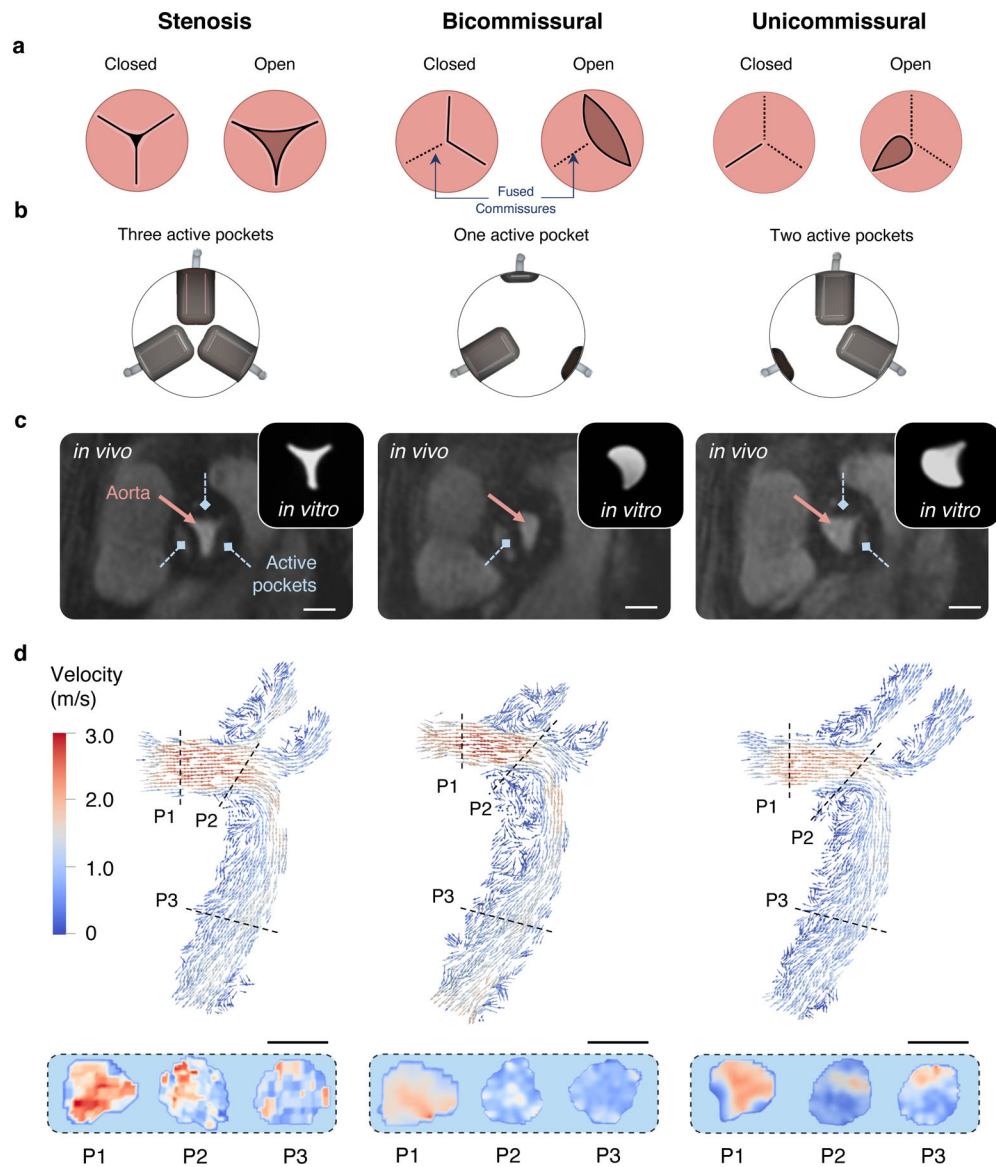
Fig. 4 |. Tunability of aortic constriction profile by varying the actuation scheme of the biomimetic soft robotic aortic sleeve and *in vivo* MRI haemodynamics.
a, Illustrations of the aortic valve in the open and closed configurations for the aortic stenosis, bicommissural, and unicommissural constriction profiles. **b,** Actuation schemes corresponding to the various constriction profiles. **c,** 2D cine MRI images of the aorta for each actuation profile *in vivo* and *in vitro*, with details of activated pockets for each condition. Scale bars, 1.2 cm. **d**, *In vivo* 2D velocity vector maps of the aorta for each constriction profile with corresponding cross-sectional planes at the ascending aorta (P1), aortic arch (P2), and descending aorta (P3) under quasi-static actuation. Scale bars, 2.0 cm.
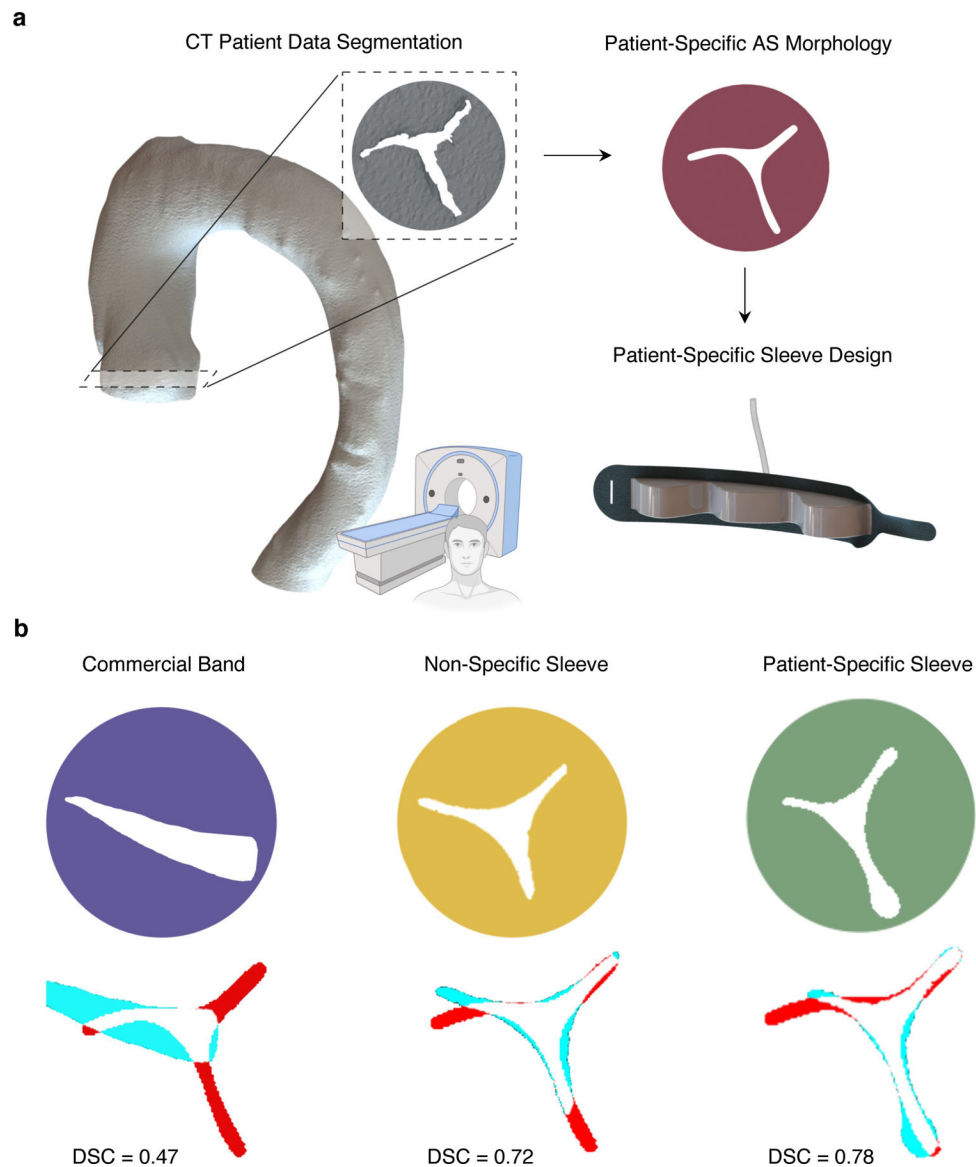
Fig. 5 |. CT-driven design of the soft robotic aortic sleeve to recapitulate patient-specific morphologies of aortic stenosis (AS).

a, Aortic segmentation from patient's CT data, with detail of the 2D projection of the aortic valve during systole. Partly created with biorender.com. **b,** Patient-specific AS morphology from CT data. **c,** Design of patient-specific aortic sleeve resulting from patient's CT data. **d-f**, Morphologies of aortic cross-sections *in vitro* resulting from aortic constriction due to **(d)** a commercial aortic banding device, **(e)** the non-specific biomimetic soft robotic aortic sleeve, and **(f)** patient-specific aortic sleeve design, and corresponding superimposed images and DSC with patient-specific AS morphology. In superimposed images, overlapping regions are shown as white, while red and cyan areas correspond to non-overlapping regions of the patient-specific AS and recreated geometries respectively.

Table 1 |
Summary of the *in vivo* haemodynamics data.

Clinical metrics for the diagnostic evaluation and staging of AS, with corresponding thresholds of mild, moderate and severe AS from the literature[31,36–38], and actuation-volume ranges of the biomimetic soft robotic sleeve used to recapitulate each metric.

	Mild		Moderate		Severe	
	Physiology metrics	Sleeve actuation (mL)	Physiology metrics	Sleeve actuation (mL)	Physiology metrics	Sleeve actuation (mL)
iEOA (cm^2/m^2)	> 0.85	< 2.0	0.6 – 0.85	2.2 – 2.8	< 0.6	> 2.8
P_{max} (mmHg)	< 40	< 2.6	40 – 65	2.6 – 3.4	> 65	> 3.4
P_{mean} (mmHg)	< 20	< 2.6	20 – 40	2.6 – 3.7	> 40	> 3.7
AS jet velocity (m/s)	< 3.0	< 2.6	3.0 – 4.0	2.6 – 3.6	> 4.0	> 3.6
ELI (cm^2/m^2)	> 1.0	< 2.3	0.5 – 1.0	2.3 – 3.3	< 0.5	> 3.3
Z_{VA} (mmHg $m^{-1}m^2$)	< 3.5	< 2.6	3.5 – 5.0	2.6 – 3.3	> 5.0	> 3.3